2025 26th International Conference on Thermal, Mechanical and Multi-Physics Simulation and Experiments in Microelectronics and Microsystems (EuroSimE) | 979-8-3503-9300-2/25/$31.00 ©2025 IEEE | DOI: 10.1109/EUROSIME65125.2025.11006609

First-principles Calculating the Stress Response of E_2(TO) Raman Phonon Deformation Potential in 4H-SiC under Mechanical Loadings

Zhoudong Yang
Shanghai Engineering Technology Research Center for SiC Power Device, Academy for Engineering & Technology, Fudan University
Shanghai, China
yangzd23@m.fudan.edu.cn

Xinyue Wang
Shanghai Engineering Technology Research Center for SiC Power Device, Academy for Engineering & Technology, Fudan University
Shanghai, China
22110860005@m.fudan.edu.cn

Yanyan Zhang
Laboratory of Advanced Materials, College of Chemistry and Materials, Fudan University
Shanghai, China
22213010013@m.fudan.edu.cn

Yuanhui Zuo
Research Institute of Fudan University in Ningbo
Ningbo, China
zuo_yuanhui@fudan.edu.cn

Hongyu Tang
Shanghai Engineering Technology Research Center for SiC Power Device, Academy for Engineering & Technology, Fudan University
Shanghai, China
hongyu_tang@fudan.edu.cn

Xuejun Fan
Department of Mechanical Engineering, Lamar University
Beaumont, USA
xfan@lamar.edu

Guoqi Zhang
EEMCS Faculty, Delft University of Technology
Delft, the Netherlands
G.Q.Zhang@tudelft.nl

Jiajie Fan*
Shanghai Engineering Technology Research Center for SiC Power Device, Academy for Engineering & Technology, Fudan University
Shanghai, China
Research Institute of Fudan University in Ningbo
Ningbo, China
*Corresponding: jiajie_fan@fudan.edu.cn

***Abstract*—4H-SiC is widely employed in power electronic devices operating under high frequencies, voltages, and temperatures due to its exceptional physical properties. However, its inherent high hardness and elastic modulus induce inevitable residual stress during device fabrication. Raman spectroscopy, which leverages lattice dynamics, offers an effective, non-destructive, rapid, and contactless method for measuring these stresses. Nevertheless, its accuracy critically depends on precisely determining the Raman phonon deformation potential constant. This work investigates mechanically induced Raman shifts in 4H-SiC via first-principles calculations and in-situ Raman spectroscopy under hydrostatic and non-hydrostatic stress conditions. The E_2(TO) and A_1(LO) phonon modes exhibit sensitivity to hydrostatic stress, whereas A_1(LO) remains largely unaffected under shear, reflecting directional vibrational differences. Theoretical predictions and experimental measurements agree well within 16% error, highlighting the effectiveness of Raman-based stress detection for 4H-SiC. This integrated theoretical–experimental approach provides a robust framework for stress and strain analysis, facilitating the design and fabrication of next-generation 4H-SiC electronic devices.**

Keywords—4H-SiC, phonon deformation potential, first-principles calculation, in-situ mechanical–Raman

I. Introduction

4H-SiC is emerging as a promising wide-bandgap semiconductor for high-power and high-frequency applications owing to its superior mechanical and thermal properties[1-4]. However, its high elastic modulus often introduces significant residual stress during device manufacturing, leading to surface cracks, structural damage, and degraded device performance[5, 6]. Therefore, there is a critical need for rapid, non-destructive techniques to detect and quantify stress in 4H-SiC. Micro-Raman spectroscopy fulfills this requirement[7], having successfully revealed residual and gradient stress in suspended microstructures of the MEMS devices[8] implantation-induced compressive stress[9-11], and stress-free regions generated by femtosecond laser processing[12]. It has also been effectively used to characterize stress states at crucial interfaces, such as Ni/Au–4H-SiC[13] and SiO_2–4H-SiC[14, 15], which are vital for device stability and reliability. Despite its promise, the accuracy of Raman-based stress detection fundamentally depends on a detailed understanding of the phonon-lattice response under various stress conditions.

The precision of micro-Raman spectroscopy for residual stress detection is inherently linked to the sensitivity of Raman-active phonons to lattice strain[16-18]. While first-principles calculations have reliably predicted Raman phonon behavior under stress for materials such as Si[19], GaN[20, 21], and AlN[20, 21], the phonon response in 4H-SiC remains inadequately explored, especially under different stress states (hydrostatic and non-hydrostatic). This research gap poses significant uncertainty and challenges for accurately detecting residual stress in 4H-SiC using Raman spectroscopy in device manufacturing. Moreover, the reliability of first-principles calculations is highly sensitive to computational parameters, such as the plane-wave cutoff energy (E_{cut}) and Brillouin zone sampling grids (Monkhorst–Pack grids). Under the Born–Oppenheimer approximation (T $\approx$0 K), optimizing these parameters is essential to accurately

979-8-3503-9300-2/25/$31.00 ©2025 IEEE Presented at the EuroSimE 2025 Conference

determine the phonon deformation potential constants of 4H-SiC without incurring prohibitive computational costs.

In this study, we systematically optimize E_{cut} and Monkhorst-Pack grids for 4H-SiC, then apply these refined settings to compute the Raman-active phonon modes in 4H-SiC under hydrostatic and non-hydrostatic pressures (biaxial, uniaxial, and shear) through first-principles calculations. The results reveal that the optical Raman phonon modes E_2(TO) and A_1(LO) modes are susceptible to stress compared to acoustic modes. Specifically, the E_2(TO) mode is more responsive to in-plane strain, while the A_1(LO) mode is more sensitive along the *c*-axis, reflecting their distinct vibrational characteristics. Furthermore, a close agreement between experimental measurements and theoretical predictions underscores the reliability of Raman spectroscopy for stress analysis in 4H-SiC device manufacturing. This work provides an important theoretical foundation for employing Raman spectroscopy in residual stress detection during 4H-SiC fabrication, facilitating more comprehensive assessments of stress, strain, and associated failure mechanisms in practical manufacturing processes.

II. Methodology

A. First Principles Calculations

First-principles calculations based on density functional theory (DFT) and the plane-wave pseudopotential method were carried out using Material Studio software's Cambridge Sequential Total Energy Package (CASTEP) module. To accurately capture systems with strong electron correlation effects, the Perdew–Wang (PW91) version of the generalized gradient approximation (GGA) was selected, as it generally provides superior accuracy compared to the local density approximation (LDA). Electron–ion interactions were described using conservative pseudopotentials. The calculation parameters included a plane-wave cutoff energy E_{cut} = 130 Ry (1678 eV), an 11 × 11 × 11 Monkhorst–Pack grid for Brillouin zone (BZ) sampling, a fast Fourier transform (FFT) grid density of 32 × 32 × 108, and an energy convergence criterion of 5×10^{-7} atomic units (a.u.). Geometry optimizations updated both the crystal lattice parameters and atomic coordinates, with convergence thresholds of 5×10^{-6} eV/atom for energy, 0.01 eV/Å for maximum force, 0.02 GPa for maximum stress, and 5×10^{-4} Å for maximum displacement. After geometry optimization, the Raman phonon frequency shift of 4H-SiC under different stress states was calculated using a hybrid approach combining finite displacement and density functional perturbation theory (DFPT). For stress loading, the [1−100], [11−20], and [0001] directions were defined as the X, Y, and Z axes, respectively, with stresses applied along these directions denoted as $\Delta\sigma_{xx}$, $\Delta\sigma_{yy}$, and $\Delta\sigma_{zz}$ (Fig. 1). When $\Delta\sigma_{xx} = \Delta\sigma_{yy} = \Delta\sigma_{zz}$, the system is under hydrostatic stress ($(\Delta\sigma_{xx} + \Delta\sigma_{yy} + \Delta\sigma_{zz})/3$); if $\Delta\sigma_{xx} \neq \Delta\sigma_{yy}$ or $\Delta\sigma_{zz}$, the system experiences non-hydrostatic stress. The effects of hydrostatic, biaxial, uniaxial, and shear loading on the Raman phonon mode of 4H-SiC were systematically calculated.

B. In-situ Mechanical–Raman Spectroscopy

In our experiments, an in-situ mechanical testing system was integrated with a micro-Raman spectrometer to capture real-time Raman phonon frequency shifts under hydrostatic and shear stress conditions. The system was initially calibrated using the single-crystal silicon peak at 520.7 cm^{-1}. Optical signals were collected through a 100× long working distance objective, equipped with a grating of 1800 gr mm^{-1}, and excited by a 532 nm laser. The laser power was maintained at approximately 5% of its full intensity to minimize potential sample heating.

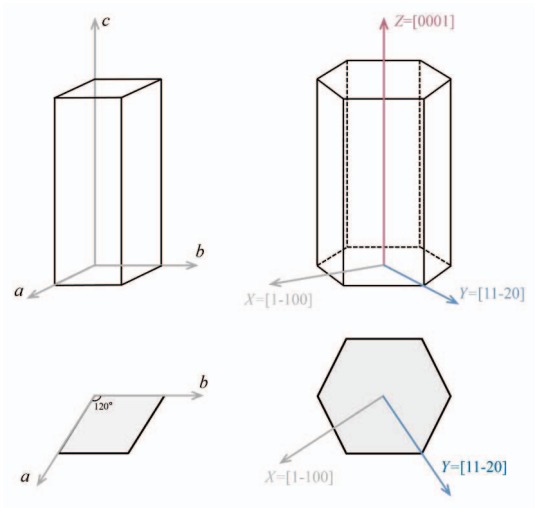

Fig. 1. Schematic of the construction of 4H-SiC crystal coordinate system and experimental coordinate system.

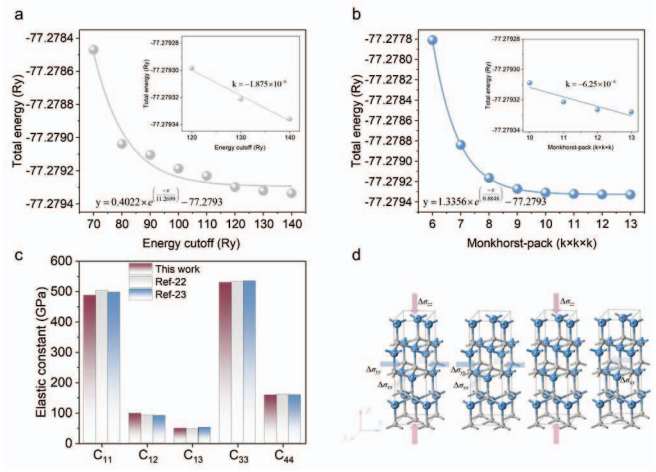

Fig. 2. Calculated parameter optimization and elastic modulus: (a) Convergence test of cutoff energy; (b) Convergence test of k-point grid. (c) Comparison between the theoretically calculated 4H-SiC elastic modulus tensor values and the results reported in the current literature; (d) Schematic diagram of the stress action mode.

TABLE I. The Elastic Constants of 4H-SiC Material Obtained by Calculation (Unit: GPa)

	C_{11}	C_{12}	C_{13}	C_{33}	C_{44}
This work	487	97.9	48.4	529.5	158.7
Ref-22	503	92	48	533	161
Relative error	3.3%	6.0%	0.8%	0.7%	1.4%
Ref-23	498	91	52	535	159
Relative error	2.3%	7.0%	7.4%	1.0%	0.2%

III. Results and Discussions

A. Cut-off Energy and Meshing Determination

Selecting an appropriate plane-wave cutoff energy (E_{cut}) is often challenging in first-principles calculations. To establish a suitable E_{cut} for 4H-SiC, we examined the impact of various E_{cut} values on the total energy following geometric

optimization, as shown in Fig. 2a. While the total energy decreases with increasing E_{cut}, the reduction rate gradually decreases after E_{cut} = 130 Ry, indicating negligible improvements in accuracy at higher cutoff energies. Additionally, because direct integration over the Brillouin zone (BZ) is computationally intensive, the Monkhorst–Pack scheme was adopted for k-point sampling. This approach exploits the crystal's translational symmetry, replacing exhaustive BZ integration with a finite set of k-points while preserving accuracy. Nonetheless, determining an optimal k-point grid for 4H-SiC remains critical. To determine an optimal value, we investigated the effect of varying k-points on the total energy, as shown in Fig. 2b. As the number of k-points increases, the total energy of the system converges rapidly and reaches an equilibrium beyond a certain threshold.

To further refine the E_{cut} and k-point mesh, we performed curve fitting and evaluated tangent slopes at different points on the energy convergence curves. The results reveal that the slope of the total energy change is on the order of magnitude (~10^{-6}) at E_{cut} = 130 Ry and an 11 × 11 × 11 k-point grid yield. Considering the balance between computational cost and accuracy, these values were selected for all subsequent calculations, including determining Raman phonon frequency shifts and phonon deformation potential constants for 4H-SiC under both hydrostatic and non-hydrostatic stress conditions. To validate the computational approach, we computed the 4H-SiC elastic tensor via GGA–PW91 and obtained values within 8% of reported experimental data[22, 23] as shown in Fig. 2c and Table I, confirming the reliability of our parameters.

B. Phonon Deformation Potential-Stress Response

The unit cell of 4H-SiC belongs to the space group $P_{63}mc$ and point group C_{6v}, as shown in Fig. 3. After geometric optimization, the strain-free lattice constants are found to be $a = b$ = 3.0965 Å and c =10.1378 Å. Based on the lattice dynamics equations and Raman stress relationships, the specific numerical relationship between phonon frequency shift and stress for 4H-SiC was determined, which depends on the Raman tensor properties for each phonon mode. The Raman tensors for E_2(TO) and A_1(LO) are[24]:

$$R_{A_1}=\begin{pmatrix} a & 0 & 0\\ 0 & a & 0\\ 0 & 0 & b\end{pmatrix}$$
$$R^1_{E_2}=\begin{pmatrix} 0 & d & 0\\ d & 0 & 0\\ 0 & 0 & 0\end{pmatrix}, R^2_{E_2}=\begin{pmatrix} d & 0 & 0\\ 0 & -d & 0\\ 0 & 0 & 0\end{pmatrix} \quad (1)$$

Thus, the phonon frequency shift for E_2(TO) and A_1(LO), induced by the stress tensor, can be expressed using the following relationship[25]:

$$\begin{aligned}\Delta\omega_{E_2} &= a_{E_2}\left(\varepsilon_{xx}+\varepsilon_{yy}\right)+b_{E_2}\varepsilon_{zz}\\ &\pm c_{E_2}\sqrt{\left(\varepsilon_{xx}-\varepsilon_{yy}\right)^2+4\varepsilon_{xy}^2}\\ \Delta\omega_{A_1} &= a_{A_1}\left(\varepsilon_{xx}+\varepsilon_{yy}\right)+b_{A_1}\varepsilon_{zz}\end{aligned} \quad (2)$$

where a_i, b_i, and c_i (i = A_1 or E_2) are the phonon deformation potential (PDP) coefficients, with the unit of cm^{-1}.

Using generalized Hooke's law, the constitutive relationship for the deformation of 4H-SiC under stress can be represented as[26]:

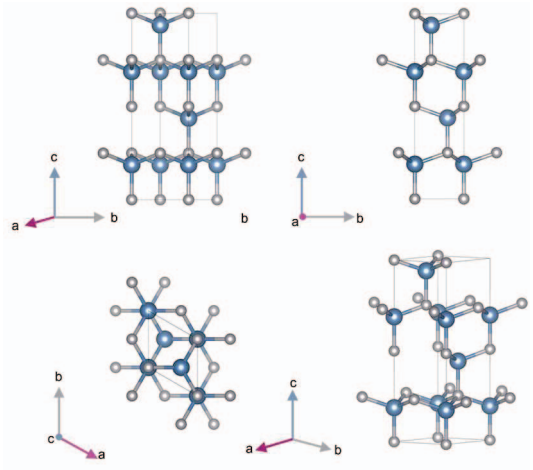

Fig. 3. Schematic of the crystal structure of 4H-SiC.

$$\begin{pmatrix}\varepsilon_{xx}\\ \varepsilon_{yy}\\ \varepsilon_{zz}\\ 2\varepsilon_{yz}\\ 2\varepsilon_{zx}\\ 2\varepsilon_{xy}\end{pmatrix}=\begin{pmatrix} s_{11} & s_{12} & s_{13} & & & \\ s_{12} & s_{11} & s_{13} & & & \\ s_{13} & s_{13} & s_{33} & & & \\ & & & s_{44} & & \\ & & & & s_{44} & \\ & & & & & 2(s_{11}-s_{12})\end{pmatrix}\begin{pmatrix}\Delta\sigma_{xx}\\ \Delta\sigma_{yy}\\ \Delta\sigma_{zz}\\ \Delta\sigma_{yz}\\ \Delta\sigma_{zx}\\ \Delta\sigma_{xy}\end{pmatrix}$$
$$=\begin{pmatrix} s_{11}\Delta\sigma_{xx}+s_{12}\Delta\sigma_{yy}+s_{13}\Delta\sigma_{zz}\\ s_{12}\Delta\sigma_{xx}+s_{11}\Delta\sigma_{yy}+s_{13}\Delta\sigma_{zz}\\ s_{13}\Delta\sigma_{xx}+s_{13}\Delta\sigma_{yy}+s_{33}\Delta\sigma_{zz}\\ s_{44}\Delta\sigma_{yz}\\ s_{44}\Delta\sigma_{zx}\\ 2(s_{11}-s_{12})\Delta\sigma_{xy}\end{pmatrix} \quad (3)$$

Combining Equations (2) and (3), the relationship between Raman frequency shift and stress is obtained:

$$\begin{aligned}\Delta\omega_{E_2} &= \left[a_{E_2}(s_{11}+s_{12})+b_{E_2}s_{13}\right](\Delta\sigma_{xx}+\Delta\sigma_{yy})\\ &+\left(2a_{E_2}s_{13}+b_{E_2}s_{33}\right)\Delta\sigma_{zz}\\ &\pm c_{E_2}\left|s_{11}-s_{12}\right|\sqrt{(\Delta\sigma_{xx}-\Delta\sigma_{yy})^2+4\Delta\sigma_{xy}^2}\\ \Delta\omega_{A_1} &= \left[a_{A_1}(s_{11}+s_{12})+b_{A_1}s_{13}\right](\Delta\sigma_{xx}+\Delta\sigma_{yy})\\ &+\left(2a_{A_1}s_{13}+b_{A_1}s_{33}\right)\Delta\sigma_{zz}\end{aligned} \quad (4)$$

To simplify this relationship, the phonon deformation potential–stress coefficients a_i', b_i', and c_i' (i = A_1 or E_2) are defined, with units of cm^{-1} GPa^{-1}:

$$\begin{aligned} a'_{E_2} &= a_{E_2}(s_{11}+s_{12})+b_{E_2}s_{13}\\ b'_{E_2} &= 2a_{E_2}s_{13}+b_{E_2}s_{33}\\ c'_{E_2} &= c_{E_2}\left|s_{11}-s_{12}\right|\\ a'_{A_1} &= a_{A_1}(s_{11}+s_{12})+b_{A_1}s_{13}\\ b'_{A_1} &= 2a_{A_1}s_{13}+b_{A_1}s_{33}\end{aligned} \quad (5)$$

The final relationship between the phonon frequency shift and stress can be expressed as:

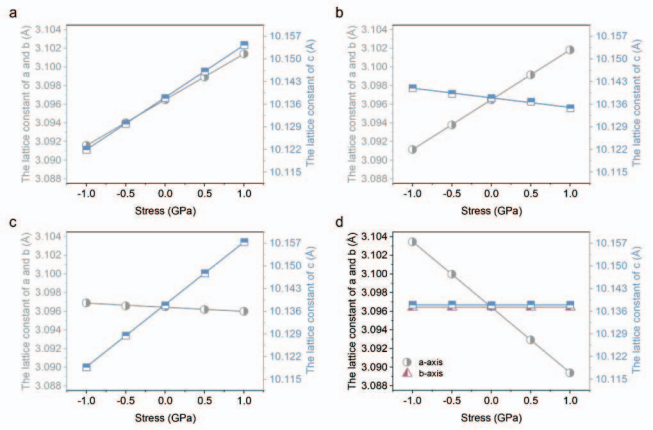

Fig. 4. Changes in lattice constants under different calculated stress modes: (a) hydrostatic stress; (b) biaxial stress; (c) Z-axis stress; (d) shear stress.

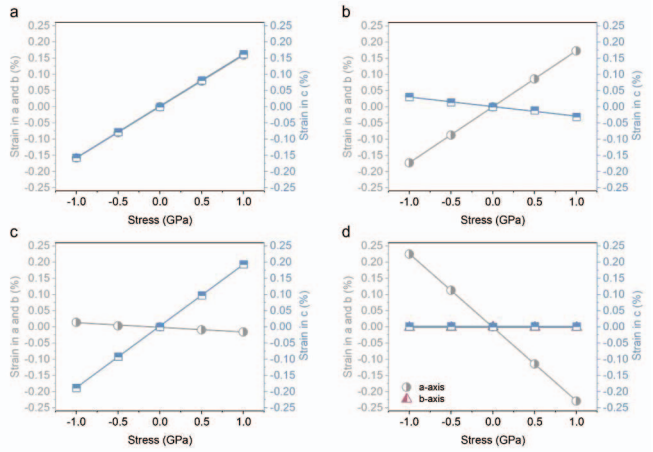

Fig. 5. Deformation under different calculation stress modes: (a) hydrostatic stress; (b) biaxial stress; (c) Z-axis stress; (d) shear stress.

$$\begin{aligned}\Delta\omega_{E_2} &= a'_{E_2}(\Delta\sigma_{xx}+\Delta\sigma_{yy})+b'_{E_2}\Delta\sigma_{zz}\\ &\pm c'_{E_2}\sqrt{(\Delta\sigma_{xx}-\Delta\sigma_{yy})^2+4\Delta\sigma_{xy}^2}\\ \Delta\omega_{A_1} &= a'_{A_1}(\Delta\sigma_{xx}+\Delta\sigma_{yy})+b'_{A_1}\Delta\sigma_{zz}\end{aligned} \tag{6}$$

This study specifically focused on four stress modes: hydrostatic stress, equibiaxial stress, uniaxial stress, and shear stress, as shown in Fig. 2d. To ensure the material remained within the elastic deformation range (satisfying Hooke's law) and the corresponding elastic deformation remained small, the frequency shift value under stress needed to be very minor relative to the stress-free frequency value (ω_0) to meeting the approximate solution requirements[27].

The simulation used a stress range of −1 GPa to 1 GPa, with negative values representing compressive stress and positive values representing tensile stress. Fig. 4 shows that within this range, the lattice constant of 4H-SiC changes linearly with different stress modes, indicating elastic behavior. Additionally, the calculated deformation in each stress mode indicates that the crystal remains in a slightly deformed state (Fig. 5).

Phonon dispersion calculations under different stress modes, as shown in Fig. 6, indicate that acoustic modes in the low-frequency region (<700 cm^{-1}) are largely unaffected by stress, whereas optical modes in the high-frequency region (>700 cm^{-1}) exhibited significant frequency shifts due to their higher sensitivity to atomic vibrations.

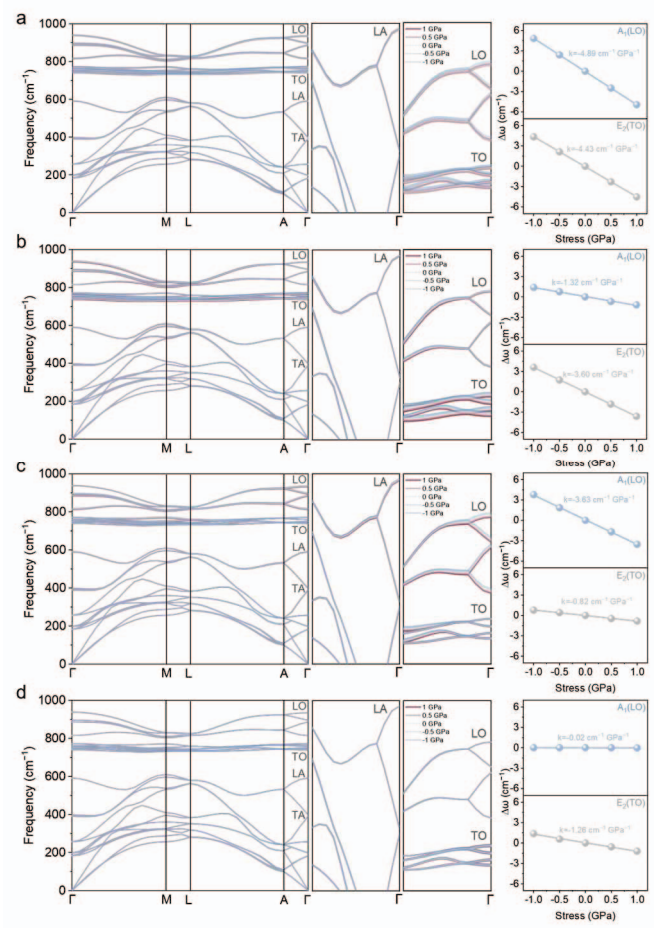

Fig. 6. Variations in Raman phonon frequencies and corresponding frequency shift–stress coefficients under different stress conditions: (a) hydrostatic stress; (b) biaxial stress; (c) Z-axis (uniaxial) stress; (d) shear stress.

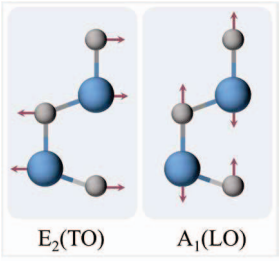

Fig. 7. Schematic diagram of the E_2(TO) and A_1(LO) phonon vibration modes.

Under hydrostatic stress, the crystal is subjected to equal stress along the X, Y, and Z axes ($\Delta\sigma_{xx} = \Delta\sigma_{yy} = \Delta\sigma_{zz} = \Delta\sigma$). At this point, the relationship between the phonon frequency shift of the E_2(TO) and A_1(LO) phonon modes and stress can be expressed as:

$$\begin{aligned}\Delta\omega_{E_2} &= a'_{E_2}(\Delta\sigma_{xx}+\Delta\sigma_{yy})+b'_{E_2}\Delta\sigma_{zz}\\ &= \left(2a'_{E_2}+b'_{E_2}\right)\Delta\sigma\\ \Delta\omega_{A_1} &= a'_{A_1}(\Delta\sigma_{xx}+\Delta\sigma_{yy})+b'_{A_1}\Delta\sigma_{zz}\\ &= \left(2a'_{A_1}+b'_{A_1}\right)\Delta\sigma\end{aligned} \tag{7}$$

In the stress range of −1 GPa to 1 GPa, as shown in Fig. 6a, the phonon frequency shifts of E_2(TO) and A_1(LO) were linearly fitted using the least squares method, yielding

phonon frequency shift-stress coefficients of −4.43 and −4.89 cm^{-1} GPa^{-1}, respectively.

In the equibiaxial stress mode ($\Delta\sigma_{xx} = \Delta\sigma_{yy} = \Delta\sigma$, $\Delta\sigma_{zz} = 0$), Equation (6) can be simplified to:

$$\begin{aligned}\Delta\omega_{E_2} &= a'_{E_2}(\Delta\sigma_{xx} + \Delta\sigma_{yy}) = 2a'_{E_2}\Delta\sigma \\ \Delta\omega_{A_1} &= a'_{A_1}(\Delta\sigma_{xx} + \Delta\sigma_{yy}) = 2a'_{A_1}\Delta\sigma\end{aligned} \tag{8}$$

The relationship between the phonon frequency shift and stress under equibiaxial stress is shown in Fig. 6b, resulting in $2a_{E2}' = -3.60$ cm^{-1} GPa^{-1} and $2a_{A1}' = -1.32$ cm^{-1} GPa^{-1}.

In the uniaxial stress mode along the Z-direction ($\Delta\sigma_{xx} = \Delta\sigma_{yy} = 0$, $\Delta\sigma_{zz} \neq 0$), Equation (6) becomes:

$$\begin{aligned}\Delta\omega_{E_2} &= b'_{E_2}\Delta\sigma_{zz} \\ \Delta\omega_{A_1} &= b'_{A_1}\Delta\sigma_{zz}\end{aligned} \tag{9}$$

After linearly fitting the frequency shifts of E_2(TO) and A_1(LO) under uniaxial stress along the Z-direction, $b_{E2}' = -0.82$ cm^{-1} GPa^{-1} and $b_{A1}' = -3.63$ cm^{-1} GPa^{-1} were obtained, as shown in Fig. 6c. Similarly, Fig. 6d depicts the dependence of phonon frequency on pure shear stress $\Delta\sigma_{xy}$. In the pure shear stress mode ($\Delta\sigma_{xx} = \Delta\sigma_{yy} = \Delta\sigma_{zz} = 0$), the frequency shift-stress relationship is given as:

$$\Delta\omega_{E_2} = 2c'_{E_2}\left|\Delta\sigma_{xy}\right| \tag{10}$$

where the value of $2c_{E2}'$ is 1.26 cm^{-1} GPa^{-1}.

Comparison of the frequency shift–stress coefficients for E_2(TO) and A_1(LO) across four stress modes indicates similar responses under hydrostatic pressure but pronounced disparities in anisotropic regimes. Specifically, the E_2(TO) mode exhibits enhanced sensitivity to in-plane perturbations, with its frequency shift coefficient surpassing A_1(LO) under equibiaxial stress and shear stress. Conversely, the A_1(LO) mode manifests axial dominance, showing stress susceptibility along the c-axis under uniaxial Z-direction loading–a direct consequence of their vibrational orientations (E_2(TO) vibrations are parallel to the (0001) plane, while A_1(LO) vibrations are along the *c*-axis), as shown in Fig. 7.

Additionally, comparing the phonon deformation potential-stress coefficients a_i' and b_i' ($i = A_1$ or E_2) under the different stress modes with those under hydrostatic pressure. The results show that the influence of different stress modes on these coefficients is negligible, allowing a single set of constants to be applied across different stress conditions. This result simplifies the interpretation of Raman-based stress analyses for 4H-SiC devices and underscores the robustness of using one deformation potential value for various loading scenarios.

C. In-situ Mechanical–Raman and Verification

To validate the phonon deformation potential results obtained from first-principles calculations, we conducted in-situ mechanical micro-Raman tests on 4H-SiC samples. This method enabled real-time monitoring of phonon frequency shifts under applied stress, providing direct experimental validation of the theoretical predictions.

Under hydrostatic stress from 0 to −1 GPa, both E_2(TO) and A_1(LO) modes exhibited blue shifts with increasing compressive stress, consistent with theoretical predictions, as shown in Fig. 8a. Using the least squares method for linear fitting, we determined the frequency-stress coefficients for E_2(TO) and A_1(LO) as −4.00 cm^{-1} GPa^{-1} and −4.55 cm^{-1} GPa^{-1}, respectively[28]. Shear stress tests showed that only E_2(TO) exhibited a frequency shift, while A_1(LO) remained unaffected (approximately 0 cm^{-1} GPa^{-1}), as shown in Fig. 8b. The relative errors between the theoretical and experimental frequency–shifted stress coefficients for hydrostatic and shear stress are within 10% and 16%, respectively (Table II). These results verify the reliability of our computational approach to analyze the phonon behavior and stress responses in 4H-SiC.

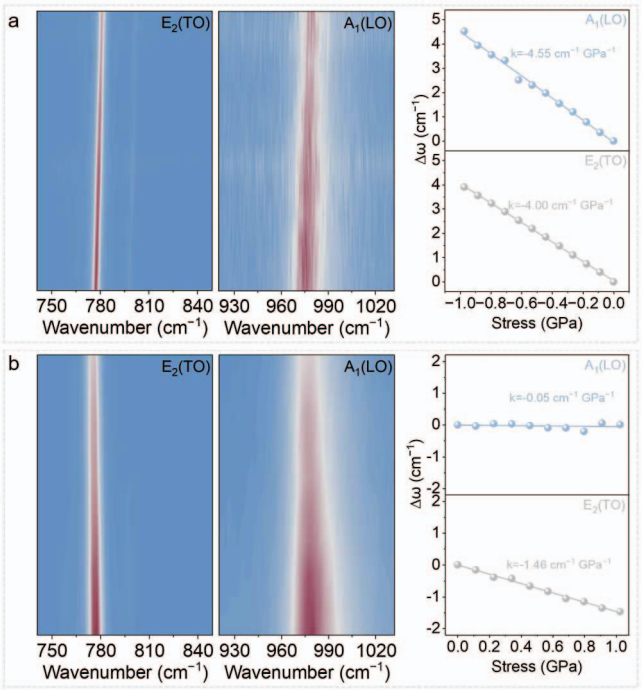

Fig. 8. In-situ Raman spectroscopy under different stress modes: (a) hydrostatic stress; and (b) shear stress.

TABLE II. THE FREQUENCY SHIFT OF EACH RAMAN VIBRATION MODE UNDER DIFFERENT STRESS MODES–STRESS COEFFICIENTS (UNIT: CM^{-1} GPA^{-1})

	i	*Hydrostatic stress*	*Shear stress*
Calculation results	E_2(TO)	−4.43	0.63
	A_1(LO)	−4.89	0.02
Experimental results	E_2(TO)	−4.00	0.73
	A_1(LO)	−4.55	0.05
Relative error	E_2(TO)	9.7%	15.9%
	A_1(LO)	7.0%	/

IV. CONCLUSION

In summary, this study optimized key computational parameters to systematically investigate the mechanically induced Raman shifts in 4H-SiC under hydrostatic, biaxial, uniaxial, and shear stress. The results indicate that the phonon deformation potentials for the E_2(TO) and A_1(LO) modes exhibit negligible variation across different stress states. Notably, the E_2(TO) mode demonstrates more sensitivity to in-plane stress, while the A_1(LO) mode primarily responds to stress along the *c*-axis. The in-situ mechanical loading experiments combined with micro-Raman spectroscopy corroborates the theoretical predictions, with discrepancies remaining within acceptable limits. These

results establish a robust theoretical and experimental framework for Raman-based stress detection in 4H-SiC device manufacturing and provide valuable insights for investigating the phonon-stress response in other materials.

ACKNOWLEDGMENT

This research was supported by the National Natural Science Foundation of China (Grant number: 52275559).

REFERENCES

[1] X. Chen *et al.*, "Research progress of large size SiC single crystal materials and devices," *Light Sci Appl,* vol. 12, no. 1, p. 28, Jan 24 2023.

[2] X. Wang *et al.*, "Effect of epoxy resin addition on properties and corrosion behavior of sintered joints in power modules serviced offshore," *J. Mater. Res. Technol.,* vol. 25, pp. 6593-6612, 2023.

[3] M. Buffolo *et al.*, "Review and Outlook on GaN and SiC Power Devices: Industrial State-of-the-Art, Applications, and Perspectives," *IEEE Trans. Electron Devices,* vol. 71, no. 3, pp. 1344-1355, 2024.

[4] X. Wang *et al.*, "Microstructure evolution and micromechanical behavior of solvent-modified Cu–Ag composite sintered joints for power electronics packaging at high temperatures," *J. Mater. Res. Technol.,* vol. 30, pp. 8433-8450, 2024.

[5] B. Hu *et al.*, "Failure and Reliability Analysis of a SiC Power Module Based on Stress Comparison to a Si Device," *IEEE Trans. Device Mater. Reliab.,* vol. 17, no. 4, pp. 727-737, 2017.

[6] H. Sakakima, A. Goryu, A. Kano, A. Hatano, K. Hirohata, and S. Izumi, "Modeling the effect of mechanical stress on bipolar degradation in 4H-SiC power devices," *J. Appl. Phys.,* vol. 128, no. 2, p. 025701 2020.

[7] Z. Yang *et al.*, "Residual Stress Characterization in Microelectronic Manufacturing: An Analysis Based on Raman Spectroscopy," *Laser & Photonics Rev.,* vol. 18, no. 7, p. 2301300, 2024.

[8] C. Wells *et al.*, "Stress and thermal characterization of 4H-SiC microelectromechanical structures," *Mater. Lett.,* vol. 191, pp. 196-199, 2017.

[9] K. Piskorski, M. Guziewicz, M. Wzorek, and L. Dobrzański, "Investigation of Al- and N-implanted 4H–SiC applying visible and deep UV Raman scattering spectroscopy," *AIP Adv.,* vol. 10, no. 5, p. 2401033, 2020.

[10] S. Yang, S. Tokunaga, M. Kondo, Y. Nakagawa, and T. Shibayama, "Non-destructive evaluation of the strain distribution in selected-area He^+ ion irradiated 4H-SiC," *Appl. Surf. Sci.,* vol. 500, p. 144051, 2020.

[11] Q. Kang *et al.*, "Improvement mechanism of brittle-plastic transition and residual stress in scratching 4H–SiC implanted by hydrogen ions," *Ceram. Int.,* vol. 48, no. 18, pp. 27076-27087, 2022.

[12] H. Shi *et al.*, "Investigation of structural transformation and residual stress under single femtosecond laser pulse irradiation of 4H–SiC," *Ceram. Int.,* vol. 48, no. 17, pp. 24276-24282, 2022.

[13] J. Suda, S. Suwa, S. Mizuno, K. Togo, and Y. Mastuo, "Micro-Raman imaging on 4H-SiC in contact with the electrode at room temperature," *Spectrochim Acta A Mol Biomol Spectrosc,* vol. 193, pp. 393-396, Mar 15 2018.

[14] W. Fu, A. Kobayashi, H. Yano, A. Ueda, S. Harada, and T. Sakurai, "Investigation of stress at SiO_2/4H-SiC interface induced by thermal oxidation by confocal Raman microscopy," *Jpn. J. Appl. Phys.,* vol. 58, no. SB, p. SBBD03, 2019.

[15] M. Yoshikawa, Y. Fujita, and M. Murakami, "Stress Characterization of the Interface Between Thermal Oxide and the 4H-SiC Epitaxial Layer Using Near-Field Optical Raman Microscopy," *Appl Spectrosc,* vol. 73, no. 10, pp. 1193-1200, Oct 2019.

[16] R. Sugie and T. Uchida, "Determination of stress components in 4H-SiC power devices via Raman spectroscopy," *J. Appl. Phys.,* vol. 122, no. 19, p. 195703, 2017.

[17] L. Ma, X. Fan, and W. Qiu, "Polarized Raman spectroscopy-stress relationship considering shear stress effect," *Opt Lett,* vol. 44, no. 19, pp. 4682-4685, Oct 1 2019.

[18] B. Han *et al.*, "Raman Characterization of the In-Plane Stress Tensor of Gallium Nitride," *Materials (Basel),* vol. 16, no. 6, p. 2255, Mar 10 2023.

[19] Z. Li, P. Graziosi, and N. Neophytou, "Deformation potential extraction and computationally efficient mobility calculations in silicon from first principles," *Phys. Rev. B,* vol. 104, no. 19, p. 195201, 2021.

[20] J. M. Wagner and F. Bechstedt, "Phonon deformation potentials of α-GaN and -AlN: An ab initio calculation," *Appl. Phys. Lett.,* vol. 77, no. 3, pp. 346-348, 2000.

[21] J. M. Wagner and F. Bechstedt, "Electronic and Phonon Deformation Potentials of GaN and AlN: Ab initio Calculations versus Experiment," *physica status solidi (b),* vol. 234, no. 3, pp. 965-969, 2002.

[22] L. Pizzagalli, "Stability and mobility of screw dislocations in 4H, 2H and 3C silicon carbide," *Acta. Mater.,* vol. 78, pp. 236-244, 2014.

[23] M. Nuruzzaman, M. A. Islam, M. A. Alam, M. A. H. Shah, and A. M. M. T. Karim, "Structural, elastic and electronic properties of 2H- and 4H-SiC," *Int. J. Eng. Res. Appl.,* vol. 5, no. 5, pp. 48-52, 2015.

[24] X. Qin *et al.*, "Raman scattering study on phonon anisotropic properties of SiC," *J. Alloys Compd.,* vol. 776, pp. 1048-1055, 2019.

[25] Z. Yang *et al.*, "Prediction of Temperature-Dependent Stress in 4H-SiC Using In Situ Nondestructive Raman Spectroscopy Characterization," *Laser & Photonics Rev.,* p. 2401033, 2024.

[26] J. Chen, A. Fahim, J. C. Suhling, and R. C. Jaeger, "A Study of the Elastic Constants of 4H Silicon Carbide (4H-SiC)," presented at the 2019 18th IEEE Intersociety Conference on Thermal and Thermomechanical Phenomena in Electronic Systems (ITherm), Las Vegas, NV, USA, 28-31 May 2019, 2019.

[27] L. Ma, W. Qiu, and X. Fan, "Stress/strain characterization in electronic packaging by micro-Raman spectroscopy: A review," *Microelectron. Reliab.,* vol. 118, p. 114045, 2021.

[28] J. Zhang *et al.*, "Effect of hexagonality on the pressure-dependent lattice dynamics of 4H-SiC," *New J. Phys.,* vol. 24, no. 11, p. 113015, 2022.